IEEE Access
Multidisciplinary | Rapid Review | Open Access Journal

Date of publication xxxx 00, 0000, date of current version xxxx 00, 0000.

Digital Object Identifier 10.1109/ACCESS.2022.Doi Number

Fish as a deformable solid: an innovative method to characterise fish swimming behaviour on acoustic videos

A. LE QUINIO[1,2,3], F. MARTIGNAC[2,4], A. GIRARD[3], J. GUILLARD[5], J-M. ROUSSEL[2,4], E. DE OLIVEIRA[1]

[1]EDF R&D LNHE – Laboratoire National d'Hydraulique et Environnement, Chatou, France
[2]UMR DECOD (Ecosystem Dynamics and Sustainability), Institut Agro, IFREMER, INRAE, Rennes, France
[3]EDF R&D PRISME – Performance, Risques Industriels et Surveillance pour la Maintenance et l'Exploitation, Chatou, France
[4]Pole MIAME, Management of Diadromous Fish in Their Environment, OFB, INRAE, Institut Agro, University Pau & Pays Adour/E2S UPPA, Rennes, France
[5] Univ. Savoie Mont Blanc, INRAE, CARRTEL, 74200 Thonon-les-Bains, France.
Corresponding author: A. LE QUINIO (e-mail: azenor.le-quinio@edf.fr).
This study was supported by Electricité de France and the French Association Nationale de la Recherche et de la Technologie.

ABSTRACT Acoustic cameras are increasingly used for continuous, non-intrusive recording and counting of fish passage in natural environments and artificial structures such as fishways. However, analysing the large number of videos recorded is time consuming. Although automatic reading processes have been developed, the poor quality of acoustic images, including discontinuity of the signal for a single object, is challenging. We developed an innovative method for analysing acoustic videos. Unlike previous methods, it focuses on swimming locomotion instead of the morphological properties of fish. Each image of a fish is pre-processed to remove discontinuities and restore the entire fish body as a single cluster of pixels. The set of pixels is then tracked to retrieve movement, independent of the displacement of the fish, using a mesh and a solid deformable model. The deformation to which the mesh is subjected between each pair of frames (i.e., deformation of the fish body) is summarised in a deformation map for each fish passage. Testing the method using a dataset of four species strongly suggested that deformation maps are species-dependent. These results must be extended to other species to confirm the effectiveness of the method for automatic identification of fish species and characterisation of their behaviour using acoustic camera records.

INDEX TERMS Acoustic video, Deformable model, Mathematical morphology, Species identification, Swimming mode

I. INTRODUCTION

Acoustic cameras (AC) are widely used for underwater surveillance, from military applications, for which they were initially designed, to monitoring of fish [1], [2] and other living organisms [3], [4]. Their high-frequency multi-beams can produce acoustic images that represent a top-down view of the ensonified volume of water, enabling two-dimensional representation of objects [5]. They can cover larger sections of water than optical cameras, while having little (e.g., turbidity) or no (e.g., luminosity) dependence on environmental conditions. Moreover, AC are non-intrusive for aquatic fauna and increasingly popular in ecological studies. They are widely used to estimate fish abundance [6], [7], [8], [9], monitor fish migration behaviour [10], [11], [12], [13], [14] and predation behaviour [15], [16] and track movement within habitats [16], [17], [18]. They provide valuable information for managing fish and fisheries, as well as hydropower plants, and for evaluating mitigation measures or assessing population stocks. However, the continuous recordings generate a large volume of data that makes reviewing them time consuming. Moreover, studies have highlighted potential bias of operators when counting fish [20], [21], [22] or measuring fish length [23], [24], [25]. In addition, the fish must be relatively large and have distinctive morphological features to be successfully identified by operators [26], [27]. Therefore, an automatic method that can analyse acoustic videos by identifying species is essential to fully exploit the potential of AC.

While automatic identification of species from optical images is already well advanced using deep-learning approaches [26], [27], [28], with some studies going as far

as identifying individual fish [31], most analysis of acoustic videos is manual [32], as computing methods are hampered by the few details available on the videos. Only characteristics related to morphology, motion and swimming locomotion can be recorded, as no information is provided on the colour or patterns of fish scales or fins. Most automated studies based on acoustic videos have focused on eel species (*Anguilla anguilla* and *Anguilla rostrata*). Because of their distinctive serpentine shape, they have been successfully distinguished from drifting debris and other species through morphological and motion analysis [33], [34], [35] and deep-learning algorithms [36], [37]. Other studies have focused on individuals of multiple species, distinguishing fish and other objects using deep-learning algorithms [38], [39], [40]. Conversely, only a few studies have distinguished multiple species with similar morphological characteristics through template matching, using acoustic shadows [41] or high-resolution images [42]. To date, these pilot studies have been conducted under controlled conditions with restrictive acquisition parameters and a range of less than 2 m, which may prevent their operational use.

These methods to automate species identification highlight the need to use another source of information available from acoustic videos: fish swimming locomotion. Hence, in addition to a diversity of morphologies, fish species also have varied modes of swimming. Studies have characterised modes of swimming based on the length and amplitude of wave propulsion [43], [44], [45]. Swimming modes can vary among species [46], although other factors can influence them, such as fish behaviour and life stage [43], [44]. For anguilliform fish, the wave propulsion pattern corresponds to a sinusoid, with nearly the entire body undulating [47]. Another major group of freshwater fish are the subcarangiforms, which undulate mainly the posterior half of the body [44]. Fish locomotion has been studied mainly in still water or steady flows [48], and current studies may increase understanding of fish movement in free-flowing water [49].

Extracting information on fish swimming locomotion from *in situ* videos is technically challenging, especially when using acoustic videos. It requires tracking the fish and quantifying its body deformation each time it is detected in the AC field of view (FOV) (i.e., in successive images). Thus, for a given point on the body, the distance between its location at two successive time steps must be measured, independent of the displacement of the fish. In this study, we explored the potential to use deformable models to decrypt and quantify the swimming locomotion of fish passing through AC FOV.

Deformable models are curves or surfaces defined from an input image [50], [51]. The models change due to internal forces within the model and external forces calculated from the processed image [52]. Deformable models are used for many image-processing applications, including image segmentation [51], object tracking [53], [54], edge detection and shape modelling [52]. First introduced by [55], a variety of deformable models have since been developed [51], [52], [56], [57], in two categories: geometric and parametric. Geometric models track the deformation using geometric measures, independent of the parametrisation, which implicitly represents the curves and surfaces [58]. Despite their simple implementation and efficient computation time [59], geometric models do not rely on physical principles, which prevents them from considering natural deformations. In comparison, parametric models explicitly represent the curves and surfaces using prior information on shape [56], which ensures direct interactions with the model [58].

Among parametric models, gradient domain mesh deformation is a surface-based, variational optimisation method (i.e., optimisation over a space of functions). It explicitly preserves local shape properties during deformation, thus avoiding the distortion that other mesh-based models generally cause [52]. To do so, the method directly encodes geometric details of the object by calculating the Laplacian from the curve's discrete points [52]. During deformation, preservation of the Laplacian coordinates also preserves the mesh details [52]. Like for many other parametric models [51], the deformation minimises energy, including internal and external terms. Internal energy terms aim to preserve the local shape properties, so that deformation of the mesh minimises divergence from the initial one. Conversely, external energy terms ensure that the mesh deforms to the desired output positions. To solve this energy-minimisation problem, nonlinear optimisation methods are usually used, as their nonlinear constraints can induce the expected deformations [52]. These gradient domain techniques have been used successfully in studies of mesh deformation [60], [61], [62].

Here, we developed a new method for analysing acoustic videos that extends beyond analysing static images of objects. We combined deformable models with computer-vision methods to quantify and track body deformation of fish passing through AC FOV. Our aim was to develop a method that can retrieve features of fish swimming locomotion from acoustic videos and to evaluate their utility for identifying species. The method's ability to distinguish species was tested using an acoustic video dataset with records of four fish species swimming through the FOV of an AC set in a free-flowing river.

II. DATA DESCRIPTION

The method was based on the passage of four individuals recorded using the Adaptive Resolution Imaging Sonar (ARIS, Sound Metrics Corp). The data were recorded at two

monitoring sites in France: the Sélune River [39], [63] and the intake canal of the Mauzac hydropower plant, on the Dordogne River [35]. Two ARIS models were used: an ARIS 1800 (96 beams) and an ARIS 3000 (128 beams). Although they had the same acquisition frequency, they had different resolutions and recording windows (9 and 14 m wide, respectively) (Table I). Due to lower water levels at the Sélune River, the videos recorded there included constant echoes from the river bottom. The AC were set up on one bank of the river, perpendicular to the water current, which projected fish passages apically on the videos and showed deformation of each fish's body as it swam (Fig. 1).

TABLE I
ACQUISITION PARAMETERS AND ACOUSTIC CAMERA SETTINGS

Monitoring site	Mauzac	Sélune
AC type	ARIS 1800	ARIS 3000
Acquisition mode	High frequency	Low frequency
Frequency (MHz)	1.8	1.8
Frame rate (frames/s)	7	5
Number of beams	96	128
Minimum range (m)	0.7	2.0
Maximum range (m)	9.4	16.0
Field-of-view opening (°)	28 × 14	28 × 15
Frame height × width (px)	1276 × 664	1350 × 738

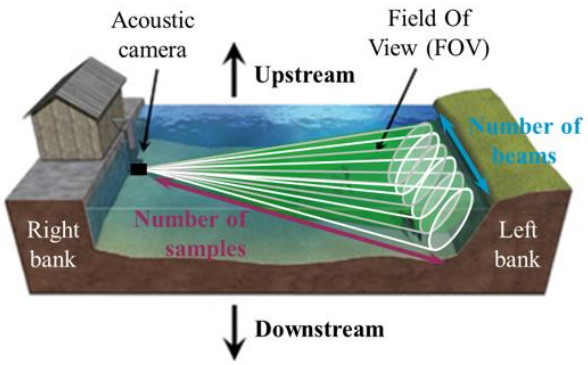

FIGURE 1. Diagram of the acoustic camera installed on the right bank of a river. The camera's recording volume is (green) determined by its multiple beams (white). Adapted from [64].

An experienced operator reviewed all videos to identify the species or group of species of each individual that crossed the AC FOV by analysing its morphological and behavioural characteristics. Four species or group of species were chosen to develop the method: the European eel (*A. anguilla*, EEL), Atlantic salmon (*Salmo salar*, SAT), European catfish (*Silurus glanis*, SIL) and a cyprinid fish (CYP) that was either a common bream (*Abramis brama*) or common carp (*Cyprinus carpio*) (Fig. 2). Their differing morphology and swimming locomotion (Table II) provided the operator with a high degree of confidence. From the highest-quality videos of passages (i.e., the fish was easily distinguishable from the background), one individual of each species or group of species was selected that swam perpendicular to the AC beams, which helped to capture body undulation in the largest number of consecutive frames (Table III).

TABLE II
MORPHOLOGY AND SWIMMING LOCOMOTION OF THE GROUP STUDIED

Group	Morphology	Swimming locomotion
European eel	Serpentine shape with uniform body distribution. Large individual (> 70 cm).	Anguilliform
Atlantic salmon	Ellipsoidal shape of the main body that becomes thinner at the caudal end. Large individual (> 70 cm).	Subcarangiform
European catfish	Serpentine shape with a head wider than the main body, with a nearly triangular shape. Large individual (> 70 cm).	Anguilliform
Cyprinid	Ellipsoidal shape of the main body that is becomes thinner at the caudal end. Small individual (< 70 cm).	Subcarangiform

TABLE III
ACQUISITION CHARACTERISTICS OF THE INDIVIDUALS STUDIED

Group	Mean length (px)	Measured length (cm)	No. of frames	Monitoring site
European eel	129	85.6	19	Mauzac
Atlantic salmon	88	75.0	14	Sélune
European catfish	115	108.0	11	Sélune
Cyprinid	70	63.8	17	Sélune

III. METHOD DEVELOPED

A. DETECTING THE TARGET'S IMAGES

Successive binary images of the fish were detected, extracted, and tracked using the method of [35]. Moving objects were isolated by smoothing the acoustic image and subtracting the background. Dilation was then applied to identify the area of interest and extract the target's binary image. However, the image of a target's body is often defined as several clusters of pixels instead of a continuous representation [35]. To maximise image information, we developed a method to restore the target's images (Fig. 3a) using a sequence of mathematical morphological filters [65] (Fig. 3).

First, a vignette with the binary image (BS) is extracted by applying the background-subtraction filter (Fig. 3b). A denoised image (F) is then obtained by removing small noise, and small occlusion through opening followed by closing, using a small (5 × 5 mm) structuring element (Fig. 3c). A clustered image (D) is then obtained by applying oriented dilation, whose structuring element has a shape that is set to follow the orientation of the target as much as possible, whether horizontal (a lying rectangle of 50 × 120 mm), vertical (a standing rectangle of 120 × 50 mm) or diagonal (a square of 120 × 120 mm) (Fig. 3d). Applying these three structuring elements to an example cluster of pixels, corresponding to a fish image with 65° orientation, highlights the benefit of using oriented dilation to exclude nearby noise (Fig. 4). The resulting noise-free targeted image (I) corresponds to the intersection of images BS and D (Fig. 3e). The processed image (R) is restored through dilation of

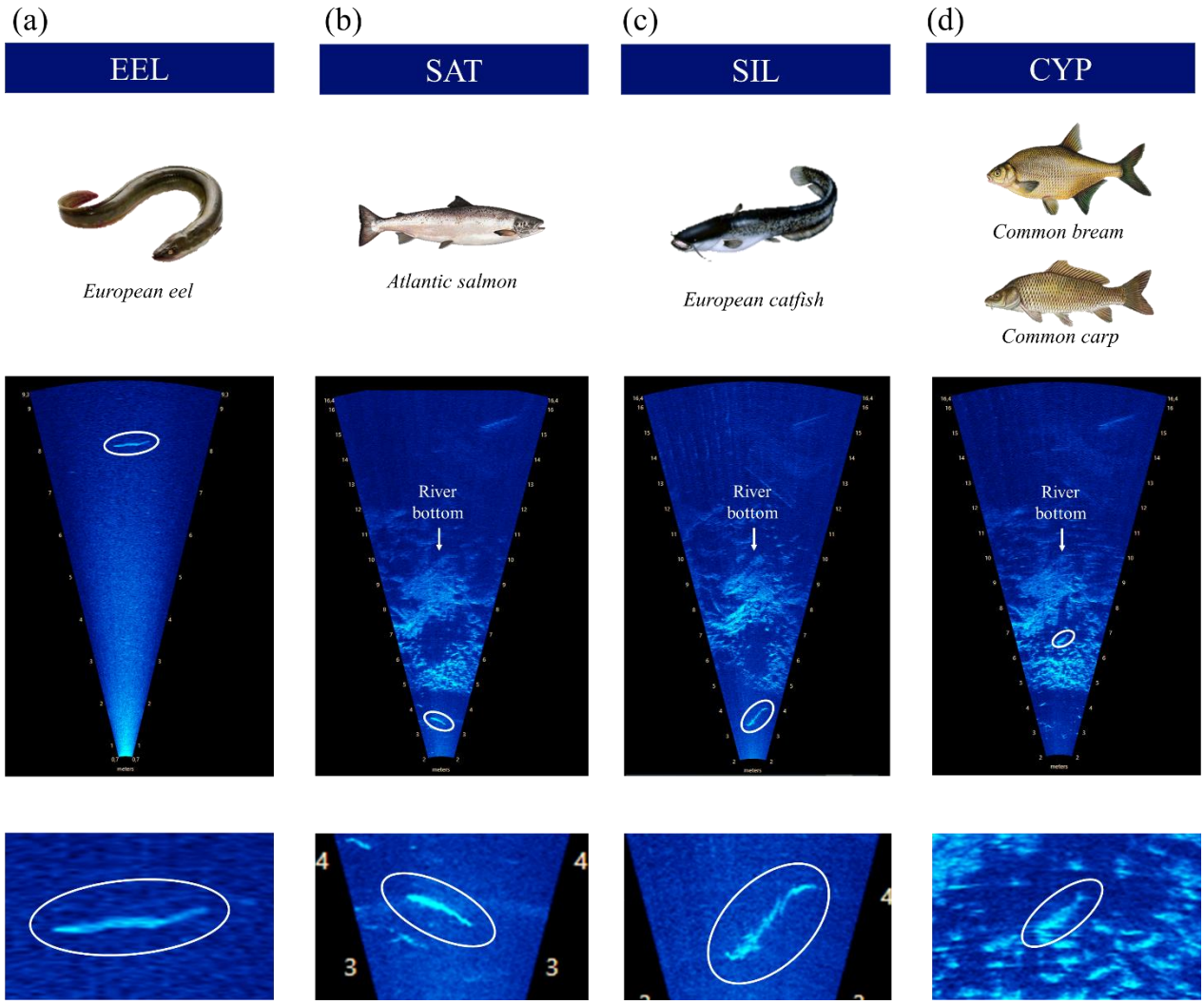

FIGURE 2. **Examples of acoustic images (full-beam in middle, close-up at bottom) captured using acoustic cameras, by species: (a) EEL, (b) SAT, (c) SIL and (d) CYP.**

image I using a structuring element, of 120 × 120 mm, corresponding to M × M pixels as a function of the frame resolution r (M = 120/r), followed by erosion of (M-1) × (M-1) pixels (Fig. 3f).

A. FOLLOWING THE TARGET'S DEFORMATION OVER TIME

To use a deformable model, the mesh to deform is first generated as a triangular mesh using the contour points of the binary shape. All coordinate points of the mesh are summarised in the scalar V. From the mesh, the N points on the outer edge of the mesh (V_b) are differentiated from the M points on the inside of the mesh (V_{inner}) (Fig. 5). Vector V_b is sorted so that the neighbours of $v_i \in V_b$ in the outer edge of the mesh are v_{i-1} and v_{i+1} (Fig. 5). For V_{inner}, a 2-column matrix (ED) is defined that contains all combinations of edges $v_i - v_j \in V_{inner}$.

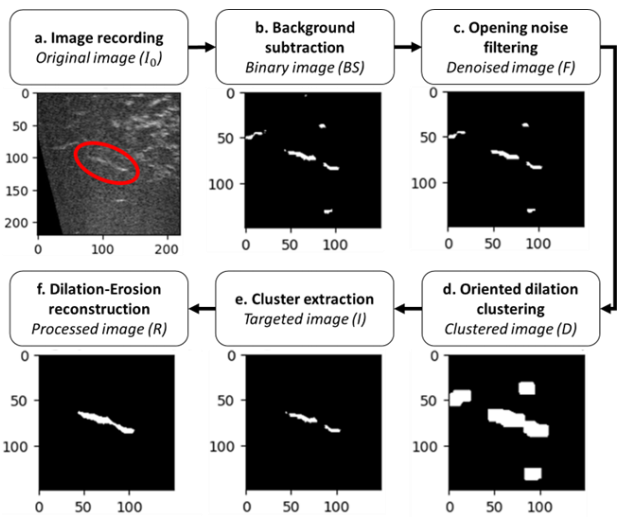

FIGURE 3. **Method used to restore the target's image. The (a) original image (red circle) was first processed using the method of [34]. Restoration begins with (b) the binary image after background subtraction. (c) Noise was filtered, and occlusion attenuated through opening followed by closing before applying (d) oriented dilation to the resulting binary image. The (e) targeted image is calculated as the intersection of the binary image and the clustered image. The (f) processed image is restored by dilating and eroding the targeted image. mesh**

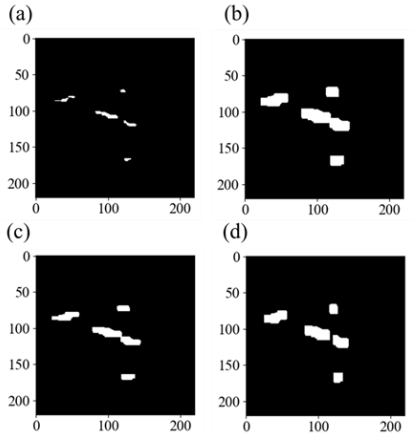

FIGURE 4. Example of (a) a noise-free vignette dilated with three structuring elements: (b) square, (c) lying rectangle or (d) standing rectangle. Because the target's orientation target is 65°, oriented dilation is performed using the square structuring element (i.e., 45°).

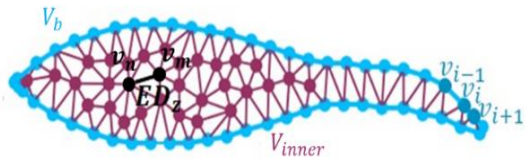

FIGURE 5. Definition of the scalars on the outer edge (V_b) (blue) and inside (V_{inner}) (pink) of the fish-image contour as well as the 2-column matrix ED. The black line corresponds to the z^{th} item of the ED matrix such as $ED_z = (v_n\ v_m)$.

The model of deformation deforms the mesh by minimising the energy of deformation (1) [61] based on the constraints set. The first three terms of (1) aim to preserve the local properties of the mesh, while the last one aims to provide the direction of the deformation.

$$||LV\text{-}\ \delta(V)||^2 + ||MV||^2 + ||HV\text{-}e(V)||^2 + ||CV\text{-}\ U||^2 \quad (1)$$

with $||LV\text{-}\ \delta(V)||^2$ aiming to preserve the overall curve of the mesh; $||MV||^2$ aiming to preserve local areas inside the mesh using mean value coordinates; $||HV\text{-}e(V)||^2$ aiming to preserve the local areas inside the mesh using edge lengths; and $||CV\text{-}U||^2$ representing the constraints on the positions for which the model must deform. These terms are explained below.

From [59]:

$$L_p(v_i) = v_i - (v_{i-1} + v_{i+1})/2 \quad (2)$$

with $v_i \in V_b$, and v_{i-1} and v_{i+1} the two neighbours of v_i in the curve.

From this, one can deduce:

$\forall\ i \in [1, N], \forall\ j \in [1,N+M]$,

$$L_{i,j} = \begin{cases} 1 & if\ i = j \\ -0.5 & if\ i = j-1 \text{ or } i = j+1 \\ 0 & else \end{cases} \quad (3)$$

Next, $\delta(V)$ is calculated as:

$$\forall\ i \in [1, N],\ \delta_i = T_i\ \delta_i^{t-1}$$

with T the transformed Laplacian calculated from t = t-1 to t = t [66].

Regarding the second and third terms of (1), based on [61], one can deduce the following:

$\forall\ i \in [N+1, N+M], \forall\ j \in [1, N+M]$,

$$M_{i,j} = \begin{cases} -w_{i,j} & if\ j \in T(i) \\ 0 & else \end{cases} \quad (4)$$

$\forall\ i \in [N+1, N+M]$,

$$M_{i,i} = -\sum_{j \in T(i)} w_{i,j} \quad (5)$$

with T(i) all points in the neighbourhood of v_i (i.e., those in the triangles for which v_i is an apex) and $w_{i,j}$ the mean value coordinates of v_i with v_j in the area formed by its neighbours and calculated from [67]:

$$w_{i,j} = (\tan(\alpha_j/2) + \tan(\alpha_{j+1}/2)) / |v_i\text{-}v_j| \quad (6)$$

with α_j the angle $v_j\widehat{v_i v_{j+1}}$, α_{j+1} the angle $v_{j+1}\widehat{v_i v_{j+2}}$ and v_{j+2} the next point in T(i) after v_j.

Concerning the third term $||HV\text{-}e(V)||^2$, minimising it maintains the edge length between two points v_n and v_m from V_{inner}. From [59]:

$$\sum_{(i,j)\epsilon E_g} \| (v_i - v_j) - e(v_i, v_j) \|^2 \quad (7)$$

with:

$\forall\ s \in [1, S]$,

$$e_s = e\left(v_{ED_{i,1}}, v_{ED_{i,2}}\right) = \frac{\tilde{l}_{ED_{i,1},ED_{i,2}}}{l_{ED_{i,1},ED_{i,2}}}\left(v_{ED_{i,1}} - v_{ED_{i,2}}\right) \quad (8)$$

with $\tilde{l}_{ED_{i,1},ED_{i,2}}$ the distance, before deformation, between the points of the i^{th} edge whose indices in V_{inner} are $ED_{i,1}$ and $ED_{i,2}$, respectively, and $l_{ED_{i,1},ED_{i,2}}$ the same distance but calculated at the current deformation step. Based on (7), matrix H is deduced:

$\forall\ i \in [1, S], \forall\ j \in [1, N + M]$,

$$H_{i,j} = \begin{cases} 1 & if\ ED_{i,1} = j \\ -1 & if\ ED_{i,2} = j \\ 0 & else \end{cases} \quad (9)$$

Regarding the fourth term $||CV\text{-}\ U||^2$, the matrix U contains the coordinates of points to which the corresponding mesh's points must tend. The method developed gives instructions only for the outer points (V_b) of the mesh:

$$\forall\ v_i \in V_b,\ v_i = u_i \quad (10)$$

with u_i the constraint at the i^{th} point of the mesh's curve. From (14), one can deduce the following:

$$\forall\ i, j \in [1, N + M],\ C_{i,j} = \begin{cases} 1 & if\ i < N\ and\ i = j \\ 0 & else \end{cases} \quad (11)$$

$$\forall\ i \in [1, N + M],\ U_i = \begin{cases} u_i & if\ i < N \\ 0 & else \end{cases} \quad (12)$$

All matrices of the deformable model are initialised before the process begins. Only matrices δ, ED, e and U are re-defined at each iteration based on the associated value of V.

Weights (α, β, γ and λ) can be applied in front of each term of the deformation energy model depending on the importance given to the corresponding criteria:

$$\alpha||LV\text{-}\ \delta(V)||^2 + \beta||MV||^2 + \gamma||HV\text{-}e(V)||^2 + \lambda||CV\text{-}\ U||^2 \quad (13)$$

B. SETTING UP POSITION CONSTRAINTS

Matrix U of the deformation from t = k-1 to t = k is defined from the coordinates (C_k) at t = k of the contour to be deformed. The contour's points that correspond to the curve's points (V_b) of the mesh are identified by calculating the curvilinear distance of (i) each point of V_b to the mesh's

origin and (ii) each point of C_k to the contour's origin (14) (Fig. 6).

$$l_{A,i} = \sum_{j=1}^{i} \| p_{j-1} - p_j \|^2 \quad (14)$$

with $l_{A,i}$ the curvilinear distance of the i^{th} point of curve A, and p_{i-1} and p_{i+1} two neighbouring points of curve A.

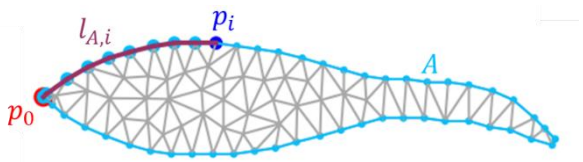

FIGURE 6. Graph of the curvilinear distance ($d_{A,i}$) (pink) for the i^{th} point (p_i) (dark blue) of curve A (light blue).

From the curvilinear distances, the matching points on C_k (Fig. 7) are identified, and matrix U of the deformation from t = k-1 to t = k is deduced:

$$\forall v_i \in V_b, U_i = \mathcal{C}_j \text{ if } l_{\mathcal{C},j} = l_{V_b,i} \quad (15)$$

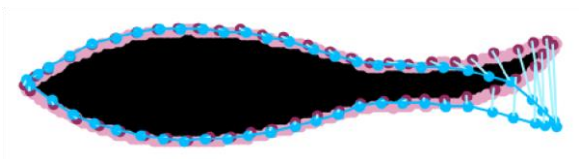

FIGURE 7. Matching of the curve's mesh at t = k-1 (blue) to the corresponding points in the image's contour at t = k+1 (pink).

C. INITIALISING THE DEFORMATION

Each deformation process is performed after the targets have been tracked. The mesh is initialised based on the target's successive images before the deformation begins. The shape used for initialisation influences the mesh's definition. To keep the method generic (i.e., disconnect the mesh's definition from the target to deform to), an initial mesh is generated from an ellipse whose major and minor axes equal the maximum lengths of those of the target's images (Fig. 8a). Next, the mesh is deformed to fit the target's reference (i.e., most representative) image (Fig. 8b, c). This image corresponds to the one whose target's length equals the 3rd quartile of the target length of all images. The resulting coordinates of the mesh define V_0, which is then used to initialise the deformation process (i.e., at t = k-1), and the process continues until it reaches the last detected image of the target. For mesh initialisation, we chose weights of the deformation energy model equal to $\alpha = \beta = \gamma = 0.8$ and $\lambda = 1$. For deformation of the remaining images, the first three weights of the position constraints were changed to $\alpha = \beta = \gamma = 0.1$.

A deformable model is not designed to address large differences, such as translation or rotation, between iterations. When these differences exist, they must be addressed separately before beginning the deformation process. First, one calculates the overall orientation of the object compared to the horizontal axis (θ), which process. First, one calculates the overall orientation of the object compared to the horizontal axis (θ), which corresponds to the ellipse that best fits the object. The object is then rotated using the corresponding matrix R (16) and translated so that its centroid (c_t) matches that in the previous time step (c_{t-1}).

$$R = \begin{pmatrix} cos\,\theta & -sin\,\theta & (1-cos\,\theta)\times c_x - sin\,\theta \times c_y \\ -sin\,\theta & cos\,\theta & sin\,\theta \times c_x + (1-cos\,\theta)\times c_y \end{pmatrix} \quad (16)$$

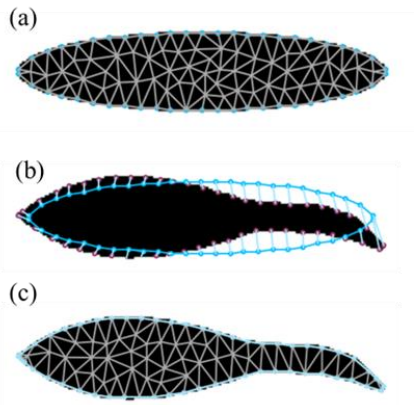

FIGURE 8. Steps used to initialise the model: (a) a mesh is generated from the ellipse, (b) the mesh is deformed to fit the contours of the reference image, (c) and the deformed mesh is used to initialise the matrices of the energy of deformation.

D. CALCULATING THE DEFORMATION

Before quantifying the deformation, the common area of the object at t = k and t = k-1 is maximised by translation to avoid incorrectly quantifying deformation due to a lack of precision during the previous iteration. Deformation between V_{k-1} and V_k can be quantified by calculating the scalar d, which equals the distance between the each of the curve's points at t = k-1 and t = k (Fig. 9):

$$\forall\, i \in V_b,\ d_i = v_i^k - v_i^{k-1} \quad (17)$$

with v_i^k and v_i^{k-1} the coordinates of the points at t = k and t = k-1, respectively.

Calculating d for each iteration generates a matrix (D), which is the deformation map of the method. Its vertical axis equals the number of detections (i.e., the time axis), while its horizontal axis equals the points on the upper curve from the head to the tail of the target plus those on the lower curve from the tail to the head.

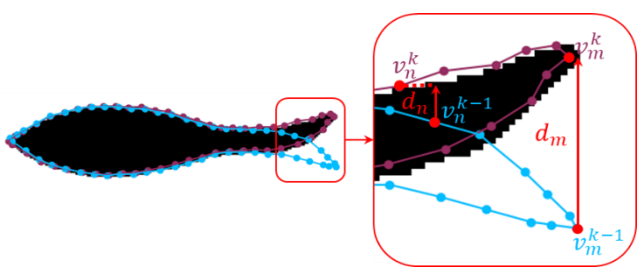

FIGURE 9. Example of two distances (d_n and d_m) between two sets of points

E. SIGNAL PROCESSING OF THE DEFORMATION MAPS

Because AC have a higher acquisition frequency than optical cameras do (i.e., mean of 5-8 vs. 24 frames per second (fps), respectively), they have a shorter period between successive detections, which might prevent them from detecting certain deformation patterns. Consequently, m points along the time axis are linearly interpolated to obtain a frame rate similar to that of optical cameras:

$$m = 24 \times N / fps \quad (18)$$

with N the initial number of frames in the deformation map and fps the frame rate of the acoustic video available in the raw data and transferred to the AVI video.

To filter noise and highlight the main patterns in the deformation map, the correlation of the deformation signal with a Gaussian function (with $\sigma = 1.5$) is calculated at each time step.

Finally, the deformation map is decomposed using principal component analysis, whose first two components are used to reconstruct the map. Doing so removes secondary components and focuses on the predominant modes that explain more than 90% of the variance in deformation maps of the entire dataset. Combining the three signal-processing steps yields a smoother signal to process.

IV. RESULTS

Body deformation varied among the four individuals selected (Fig. 10). For each image in which fish are detected, the deformation is calculated at each point of the mesh contour and collected for all points in a one-dimensional array. Visually, the array corresponds to a one-row image whose colour becomes brighter as the deformation increases. When the deformation is towards the top of the image (i.e., the mesh point was higher in the image at t = k than at t = k-1), the colour tends towards yellow, and when the deformation is towards the bottom of the image, the colour tends towards blue. The one-row image can be read from the centre outwards: its left side corresponds to points on the upper curve of the fish silhouette (from head to tail), while its right side corresponds to points on the lower curve (from tail to head). The middle of the row thus corresponds to the caudal fin, while the ends correspond to the head. All one-row images are stacked along the time axis, which creates a deformation map that describes how a fish's movement deforms its body. The deformation maps are then post-processed to analyse them (Fig. 11).

Once they are post-processed, the distribution of deformation at each point can be summarised using boxplots (Fig. 12b, d, f, h). They provided initial information on body deformation for each of the four individuals selected. For SIL and EEL, deformation occurred mainly at the caudal fin, with deformation increasing towards the tail. For SAT and CYP, although deformation was observed at the head, it was largest in the last two-thirds of the body towards the tail.

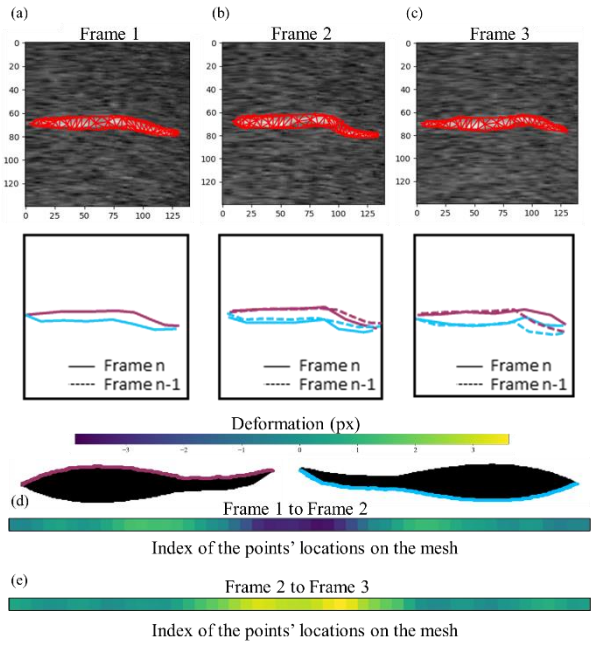

FIGURE 10. Successive (a-c) Three successive images of a fish on which the mesh (red) is superposed and the corresponding one-row images of deformation from (d) Frame 1 to Frame 2 and (e) Frame 2 to Frame 3. The left side of the one-row image corresponds to points on the lower curve of the fish silhouette, while the right side corresponds to points on the upper curve.

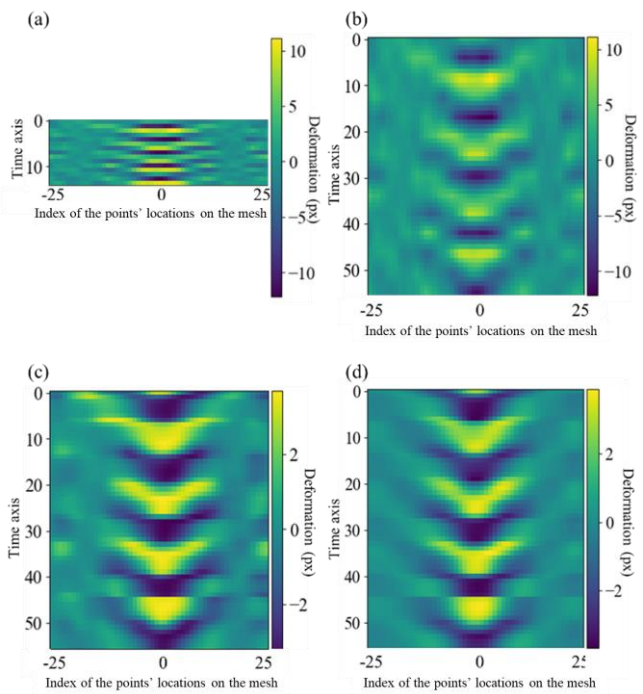

FIGURE 11. Successive processing steps of (a) a deformation map: (b) linear interpolation, (c) correlation of the signal at each time step with a Gaussian function and (d) reconstruction using the two first components of principal component analysis. The horizontal axis corresponds to the number of outer points of the deformation model, while the vertical axis corresponds to the time axis.

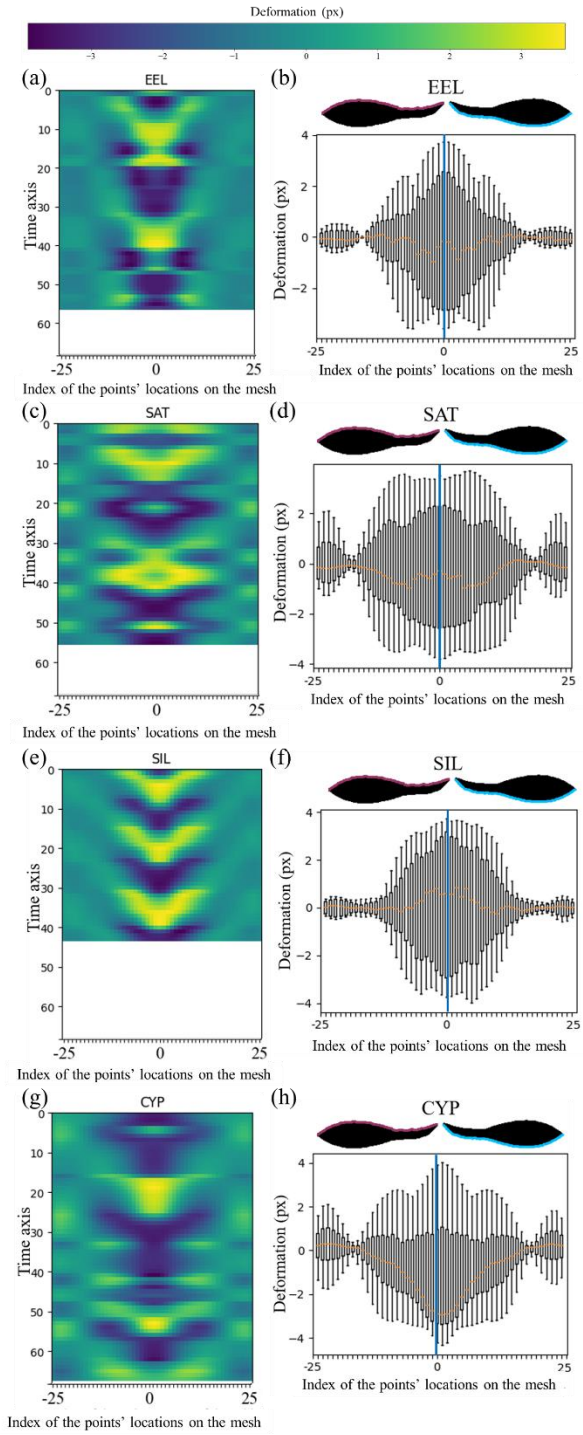

FIGURE 12. Deformation maps and corresponding boxplots for (a and b) European eel (EEL), (c and d) Atlantic salmon (SAT), (e and f) European catfish (SIL) and cyprinid fish (g and h) CYP. Whiskers equal 1.5 times the interquartile range.

Visual assessment of the deformation maps (Fig. 12a, c, d, e, g) extended these initial observations, revealing that the centre of the body of SAT and CYP regularly deformed in the direction opposite to that of the head and tail. The deformation of both individuals thus appeared similar to a beat cycle, although the CYP cycle was more heterogeneous. Conversely, each cycle of body deformation of SIL and EEL appeared to propagate, undulating along the body to the tip of the tail. The EEL cycle was longer, which reflected undulation with a larger amplitude. In addition, the deformation patterns differed between EEL and SIL (the latter more V-shaped) and between SAT and CYP (the former more diamond-shaped), although each pair had the same swimming modes.

V. DISCUSSION

Swimming locomotion is one of the main parameters with morphology that can distinguish one species from another on acoustic videos. The method we developed extracts swimming locomotion features using computer-vision methods, while applying the theory of deformable solids to acoustic images of fish. Computer-vision methods have been used for acoustic images [27], [32], similar to studies of optical images. Although deep-learning methods have been widely applied to optical images in recent years, their application to acoustic images remains limited, mainly due to the latter's low quality [30] and few clear details. Thus, automatic feature-extraction methods for acoustic videos are an essential alternative to deep learning. To the best of our knowledge, the swimming locomotion of fish in acoustic videos has never been used to identify species, despite the relevant information it can provide. Shape modelling has been considered for optical images but has not been explored to study deformation [68]. To the best of our knowledge, applying deformable models to monitor the deformation of successive fish images is original and innovative.

We used the gradient domain mesh deformable model [61], which performed well for videos in the present study and can closely follow the body contours of each fish detected in the AC FOV. The accuracy of the calculated deformation relies on the reliability of the extracted binary images of the fish. The pre-processing to remove noise and avoid occlusion in the images is essential to the method, but it could oversimplify the target's shape in the binary image or merge clusters of pixels that do not belong to an individual. If the binary image of the target is not accurate (i.e., includes pixels that do not belong to the target), the model will tend towards the wrong shape, and the calculated deformation will be inaccurate. This is a common problem due to the low quality of acoustic images, which makes them more complex to analyse than optical images. Thus, the image restoration of this method is crucial to prepare the binary images, because it reduces the disadvantages of low-quality images and negative effects on later steps of the analysis.

Post-treatment of the deformation maps is also essential to retrieve intelligible information and simplify species identification. Previous studies of swimming mode used videos from optical cameras, which have a high frame rate (24 fps, [69]) and satisfactorily follow fish body deformation during movement. Because the frame rates of the AC we

used varied from 5-8 fps, they captured body deformation erratically. Interpolating the deformation maps over time smoothed the transitions, while the filtering steps reduced noise and bias by focusing on the main characteristics of deformation. Technological research on AC has enabled manufacturers to increase the acquisition frequency of models.

Performing all steps of the method provides deformation maps that contain relevant information. The boxplots generated from the deformation maps clearly indicated that swimming modes of anguilliform species (eel and catfish) can be distinguished from those of subcarangiform species (salmon and cyprinids). Moreover, visual analysis of deformation maps highlighted the utility of studying deformation dynamics at each point and each time step, which can detect subtle differences in patterns, especially between eel and catfish and between salmon and cyprinids. Although the results are based on acoustic images of a single individual per species, they establish strong proof-of-concept and open encouraging perspectives for detecting fish species using AC records. Using deformation maps to identify species automatically requires further testing, and using larger datasets will help capture intra-species variability in fish-body deformation. Many factors can influence the deformation of a fish's body as it swims and its analysis on acoustic videos. Therefore, future research could focus on this domain, such as how swimming direction and intensity of water flow influence the propulsion energy required, and in turn how the latter deforms the body [48]. Fish behaviour, whether for hunting, migrating or foraging, modifies how the fish swims, which can influence the deformation maps. Finally, the orientation of the fish relative to the AC also influences the calculation of deformation, because it determines how much of the body length is recorded.

These factors must be considered in the analysis as they may influence the pattern, uniformity and regularity of the cycle of fish body deformation. Doing so enables reliable and useful analysis of deformation maps for identifying species as well as the study of fish swimming behaviour. Laboratory studies could help understand the main factors that influence deformation maps and provide deformation maps that could be considered as references. Finally, automating analysis of the deformation maps would help move toward automatic identification of fish species from AC records.

VI. CONCLUSION

The method developed is innovative and, to our knowledge, has never been used to identify fish species on acoustic videos. Applying deformable-solid techniques to these videos makes it possible to identify the fish's swimming mode, which is essential information that has never been used before in automatic identification methods. The information summarised in deformation maps is thus similar among individuals. We intend to enlarge our datasets and automate their analysis for identification. In addition, generating a mesh in each image in which the target is detected makes it possible to extract morphological characteristics of the fish, which is a two-for-one method for extracting features and an important advance for automatic identification of species on acoustic videos.

ACKNOWLEDGMENT

The authors thank the experienced operators who reviewed the videos and enabled identification of the species or group of species of each individual that crossed the AC FOV.

REFERENCES

[1] L. G. Rudstam, J. M. Jech, S. L. Parker-Stetter, J. K. Horne, P. J. Sullivan, and D. M. Mason, 'Fisheries Acoustics', in *Fisheries Techniques, Third edition*, A.V. Zale, D.L. Parrish, T.M. Sutton., 2012, p. 40.

[2] J. E. Simmonds and D. N. Maclennan, 'Fisheries acoustics: Theory and practice: Second edition', *Fish. Acoust. Theory Pract. Second Ed.*, pp. 1–252, Nov. 2005, doi: 10.1002/9780470995303.

[3] F. Zhao, K. Mizuno, S. Tabeta, H. Hayami, Y. Fujimoto, and T. Shimada, 'Survey of freshwater mussels using high-resolution acoustic imaging sonar and deep learning-based object detection in Lake Izunuma, Japan', *Aquat. Conserv. Mar. Freshw. Ecosyst.*, Nov. 2023, doi: 10.1002/aqc.4040.

[4] H. Rogissart, V. Frossard, J. Guillard, C. Rautureau, and S. Jacquet, 'Tracking the real-time behavior of Hemimysis anomala's winter swarms using acoustic camera', *J. Gt. Lakes Res.*, vol. 50, p. 102250, Nov. 2023, doi: 10.1016/j.jglr.2023.102250.

[5] E. O. Belcher, B. Matsuyama, and G. M. Trimble, 'Object identification with acoustic lenses', Feb. 2001, pp. 6–11 vol.1. doi: 10.1109/OCEANS.2001.968656.

[6] J. Hayes, J. Hay, I. Maxwell, and A. Quarterman, 'Estimating Trout Abundance with Cataraft-Mounted Dual-Frequency Identification Sonar: a Comparison with Drift Diving', *North Am. J. Fish. Manag.*, vol. 35, May 2015, doi: 10.1080/02755947.2015.1008114.

[7] E. A. Mora *et al.*, 'Estimating the annual spawning run size and population size of the southern distinct population segment of green sturgeon', *Trans. Am. Fish. Soc.*, vol. 147, no. 1, pp. 195–203, 2018.

[8] C. Artero *et al.*, 'High-Resolution Acoustic Cameras Provide Direct and Efficient Assessments of Large Demersal Fish Populations in Extremely Turbid Waters', *Appl. Sci.*, vol. 11, p. 1899, Feb. 2021, doi: 10.3390/app11041899.

[9] E. C. Sibley *et al.*, 'Sound sees more: A comparison of imaging sonars and optical cameras for estimating fish densities at artificial reefs', *Fish. Res.*, vol. 264, p. 106720, 2023.

[10] M. A. Kirk, C. C. Caudill, E. L. Johnson, M. L. Keefer, and T. S. Clabough, 'Characterization of adult Pacific Lamprey swimming behavior in relation to environmental conditions within large-dam fishways',

Trans. Am. Fish. Soc., vol. 144, no. 5, pp. 998–1012, 2015.

[11] F. Capoccioni, C. Leone, D. Pulcini, M. Cecchetti, A. Rossi, and E. Ciccotti, 'Fish movements and schooling behavior across the tidal channel in a Mediterranean coastal lagoon: An automated approach using acoustic imaging', *Fish. Res.*, vol. 219, Jun. 2019, doi: 10.1016/j.fishres.2019.105318.

[12] E. Lenihan, T. Mccarthy, and C. Lawton, 'Use of an acoustic camera to monitor seaward migrating silver-phase eels (*Anguilla anguilla*) in a regulated river', *Ecohydrol. Hydrobiol.*, vol. 19, Jul. 2019, doi: 10.1016/j.ecohyd.2018.07.001.

[13] E. S. Lenihan, T. K. McCarthy, and C. Lawton, 'Assessment of silver eel (*Anguilla anguilla*) route selection at a water-regulating weir using an acoustic camera', *Mar. Freshw. Res.*, vol. 72, no. 6, pp. 754–765, 2020.

[14] O. Keeken, R. Hal, H. V. Winter, I. Tulp, and A. B. Griffioen, 'Behavioural responses of eel (*Anguilla anguilla*) approaching a large pumping station with trash rack using an acoustic camera (DIDSON)', *Fish. Manag. Ecol.*, vol. 27, Apr. 2020, doi: 10.1111/fme.12427.

[15] A. Becker, A. Whitfield, P. Cowley, J. Järnegren, and T. Næsje, 'Potential effects of artificial light associated with anthropogenic infrastructure on the abundance and foraging behaviour of estuary-associated fishes', *J. Appl. Ecol.*, vol. 50, pp. 43–50, Feb. 2013, doi: 10.1111/1365-2664.12024.

[16] V. Price, P. Auster, and L. Kracker, 'Use of High-Resolution DIDSON Sonar to Quantify Attributes of Predation at Ecologically Relevant Space and Time Scales', *Mar. Technol. Soc. J.*, vol. 47, pp. 33–46, Jan. 2013, doi: 10.4031/MTSJ.47.1.6.

[17] R. Lagarde *et al.*, 'Movements of Non-Migrant European Eels in an Urbanised Channel Linking a Mediterranean Lagoon to the Sea', *Water*, vol. 13, p. 839, Mar. 2021, doi: 10.3390/w13060839.

[18] M. Bennett, A. Becker, T. Gaston, and M. Taylor, 'Connectivity of Large-Bodied Fish with a Recovering Estuarine Tidal Marsh, Revealed Using an Imaging Sonar', *Estuaries Coasts*, vol. 44, Aug. 2020, doi: 10.1007/s12237-020-00822-0.

[19] G. J. Staines, R. P. Mueller, A. C. Seitz, M. D. Evans, P. W. O'Byrne, and M. Wosnik, 'Capabilities of an acoustic camera to inform fish collision risk with current energy converter turbines', *J. Mar. Sci. Eng.*, vol. 10, no. 4, p. 483, 2022.

[20] M. L. Keefer *et al.*, 'Inter-observer bias in fish classification and enumeration using dual-frequency identification sonar (didson): A pacific lamprey case study', *Northwest Sci.*, vol. 91, no. 1, pp. 41–53, 2017.

[21] R. Lagarde *et al.*, 'In situ evaluation of European eel counts and length estimates accuracy from an acoustic camera (ARIS)', *Knowl. Manag. Aquat. Ecosyst.*, vol. 421, p. 44, Nov. 2020, doi: 10.1051/kmae/2020037.

[22] L. T. M. D. Braga, A. Giraldo, and A. L. Godinho, 'Evaluation of three methods for manually counting fish in dam turbines using DIDSON', *Hydrobiologia*, vol. 849, no. 2, pp. 309–321, 2022.

[23] J. Hightower, K. Magowan, L. Brown, and D. Fox, 'Reliability of Fish Size Estimates Obtained From Multibeam Imaging Sonar', *J. Fish Wildl. Manag.*, vol. 4, pp. 86–96, Jun. 2013, doi: 10.3996/102011-JFWM-061.

[24] A. Grote, M. Bailey, J. Zydlewski, and J. Hightower, 'Multibeam sonar (DIDSON) assessment of American shad (*Alosa sapidissima*) approaching a hydroelectric dam', *Can. J. Fish. Aquat. Sci.*, vol. 71, pp. 545–558, Apr. 2014, doi: 10.1139/cjfas-2013-0308.

[25] A. Daroux, F. Martignac, M. Nevoux, J.-L. Baglinière, D. Ombredane, and J. Guillard, 'Manual fish length measurement accuracy for adult river fish using an acoustic camera (DIDSON)', *J. Fish Biol.*, vol. 95, May 2019, doi: 10.1111/jfb.13996.

[26] R. E. Jones, R. A. Griffin, and R. K. Unsworth, 'Adaptive Resolution Imaging Sonar (ARIS) as a tool for marine fish identification', *Fish. Res.*, vol. 243, p. 106092, 2021.

[27] Y. Wei, Y. Duan, and D. An, 'Monitoring fish using imaging sonar: Capacity, challenges and future perspective', *Fish Fish.*, vol. 23, Jun. 2022, doi: 10.1111/faf.12693.

[28] A. Jalal, A. Salman, A. Mian, M. Shortis, and F. Shafait, 'Fish detection and species classification in underwater environments using deep learning with temporal information', *Ecol. Inform.*, vol. 57, p. 101088, Apr. 2020, doi: 10.1016/j.ecoinf.2020.101088.

[29] I. Yusup, M. Iqbal, and I. Jaya, 'Real-time reef fishes identification using deep learning', *IOP Conf. Ser. Earth Environ. Sci.*, vol. 429, p. 012046, Jan. 2020, doi: 10.1088/1755-1315/429/1/012046.

[30] A. Saleh, M. Sheaves, and M. Rahimi Azghadi, 'Computer vision and deep learning for fish classification in underwater habitats: A survey', *Fish Fish.*, vol. 23, Apr. 2022, doi: 10.1111/faf.12666.

[31] P. Cisar, D. Bekkozhayeva, O. Movchan, M. Saberioon, and R. Schraml, 'Computer vision based individual fish identification using skin dot pattern', *Sci. Rep.*, vol. 11, no. 1, p. 16904, Aug. 2021, doi: 10.1038/s41598-021-96476-4.

[32] R. Munnelly, J. Castillo, N. O. Handegard, M. Kimball, K. Boswell, and G. Rieucau, 'Applications and analytical approaches using imaging sonar for quantifying behavioural interactions among aquatic organisms and their environment', *ICES J. Mar. Sci.*, Nov. 2023, doi: 10.1093/icesjms/fsad182.

[33] A.-M. Mueller, T. Mulligan, and P. Withler, 'Classifying Sonar Images: Can a Computer-Driven Process Identify Eels?', *North Am. J. Fish. Manag.*, vol. 28, pp. 1876–1886, Dec. 2008, doi: 10.1577/M08-033.1.

[34] L. Bothmann, M. Windmann, and G. Kauermann, 'Realtime classification of fish in underwater sonar videos', *J. R. Stat. Soc. Ser. C Appl. Stat.*, vol. 65, p. n/a-n/a, Aug. 2016, doi: 10.1111/rssc.12139.

[35] A. Le Quinio *et al.*, 'Automatic detection, identification and counting of anguilliform fish using in situ acoustic camera data: Development of a cross-camera morphological analysis approach', *PloS One*, vol. 18, p. e0273588, Feb. 2023, doi: 10.1371/journal.pone.0273588.

[36] T. Yin, X. Zang, Z. Hou, P. Jacobson, R. Mueller, and Z. Deng, 'Bridging the Gap between Laboratory and Field Experiments in American Eel Detection Using Transfer Learning and Convolutional Neural Network', in *Proceedings of the 53rd Hawaii International Conference on System Sciences*, Jan. 2020. doi: 10.24251/HICSS.2020.116.

[37] X. Zang, T. Yin, Z. Hou, R. Mueller, Z. Deng, and P. Jacobson, 'Deep Learning for Automated Detection and Identification of Migrating American Eel Anguilla rostrata from Imaging Sonar Data', *Remote Sens.*, vol. 13, p. 2671, Jul. 2021, doi: 10.3390/rs13142671.

[38] V. Kandimalla, M. Richard, F. Smith, J. Quirion, L. Torgo, and C. Whidden, 'Automated Detection, Classification and Counting of Fish in Fish Passages With Deep Learning', *Front. Mar. Sci.*, vol. 8, Jan. 2022, doi: 10.3389/fmars.2021.823173.

[39] G. Fernandez Garcia, T. Corpetti, M. Nevoux, L. Beaulaton, and F. Martignac, 'AcousticIA, a deep neural network for multi-species fish detection using multiple models of acoustic cameras', *Aquat. Ecol.*, pp. 1–13, Jan. 2023, doi: 10.1007/s10452-023-10004-2.

[40] R. Connolly *et al.*, 'Out of the shadows: automatic fish detection from acoustic cameras', *Aquat. Ecol.*, May 2022, doi: 10.1007/s10452-022-09967-5.

[41] M. C. Langkau, H. Balk, M. Schmidt, and J. Borcherding, 'Can acoustic shadows identify fish species? A novel application of imaging sonar data', *Fish. Manag. Ecol.*, vol. 19, pp. 313–322, Aug. 2012, doi: 10.1111/j.1365-2400.2011.00843.x.

[42] Z. Yu, K. Mizuno, A. Asada, Y. Fujimoto, and T. Shimada, 'New method of fish classification by using high-resolution acoustic video camera-ARIS and local invariant feature descriptor', Sep. 2016, pp. 1–6. doi: 10.1109/OCEANS.2016.7761115.

[43] C. C. Lindsey, '1 Form, Function, and Locomotory Habits in Fish', in *Fish Physiology*, vol. 7, 1978, pp. 1–100. doi: 10.1016/S1546-5098(08)60163-6.

[44] M. Sfakiotakis, D. Lane, and J. Davies, 'Review of Fish Swimming Modes for Aquatic Locomotion', *Ocean. Eng. IEEE J. Of*, vol. 24, pp. 237–252, May 1999, doi: 10.1109/48.757275.

[45] P. W. Webb, 'Form and Function in Fish Swimming', *Sci. Am.*, vol. 251, no. 1, pp. 72–83, 1984.

[46] V. Di Santo *et al.*, 'Convergence of undulatory swimming kinematics across a diversity of fishes', *Proc. Natl. Acad. Sci.*, vol. 118, p. e2113206118, Dec. 2021, doi: 10.1073/pnas.2113206118.

[47] E. Tytell, I. Borazjani, F. Sotiropoulos, T. Baker, E. Anderson, and G. Lauder, 'Disentangling the Functional Roles of Morphology and Motion in the Swimming of Fish', *Integr. Comp. Biol.*, vol. 50, pp. 1140–54, Dec. 2010, doi: 10.1093/icb/icq057.

[48] J. Liao, 'A review of fish swimming mechanics and behaviour in altered flows', *Phil Trans R Soc B*, vol. 362, pp. 1973–1993, Dec. 2007, doi: 10.1098/rstb.2007.2082.

[49] G. Lauder, 'Fish Locomotion: Recent Advances and New Directions', *Annu. Rev. Mar. Sci.*, vol. 7, Sep. 2014, doi: 10.1146/annurev-marine-010814-015614.

[50] T. McInerney and D. Terzopoulos, 'Deformable models in medical image analysis: a survey', *Med. Image Anal.*, vol. 1, pp. 91–108, Jul. 1996, doi: 10.1016/S1361-8415(96)80007-7.

[51] C. Xu, D. Pham, and J. Prince, 'Image Segmentation Using Deformable Models', *Handb. Med. Imaging Vol. 2 Med. Image Process. Anal.*, May 2000.

[52] C. Xu, X. Han, and J. L. Prince, 'Chapter 10 - Gradient Vector Flow Deformable Models', in *Handbook of Medical Image Processing and Analysis (Second Edition)*, Second Edition., I. N. BANKMAN, Ed., Burlington: Academic Press, 2009, pp. 181–194. doi: https://doi.org/10.1016/B978-012373904-9.50018-0.

[53] Y. Zhong, A. K. Jain, and M.-P. Dubuisson-Jolly, 'Object tracking using deformable templates', *IEEE Trans. Pattern Anal. Mach. Intell.*, vol. 22, no. 5, pp. 544–549, 2000, doi: 10.1109/34.857008.

[54] S. Dambreville, Y. Rathi, and A. Tannenbaum, 'Tracking deformable objects with unscented Kalman filtering and geometric active contours', in *2006 American Control Conference*, 2006, p. 6 pp.-. doi: 10.1109/ACC.2006.1657152.

[55] D. Terzopoulos, 'On Matching Deformable Models to Images', in *Topical Meeting on Machine Vision*, Optica Publishing Group, 1987, p. FD1. [Online]. Available: https://opg.optica.org/abstract.cfm?URI=MV-1987-FD1

[56] A. K. Jain, Y. Zhong, and M.-P. Dubuisson-Jolly, 'Deformable Template Models: A Review', *Signal Process*, vol. 71, no. 2, pp. 109–129, Dec. 1998, doi: 10.1016/S0165-1684(98)00139-X.

[57] M. Selim and R. Koomullil, 'Mesh Deformation Approaches – A Survey', *J. Phys. Math.*, vol. 7, Jun. 2016, doi: 10.4172/2090-0902.1000181.

[58] P. Mesejo, A. Valsecchi, L. Marrakchi-Kacem, S. Cagnoni, and S. Damas, 'Biomedical image segmentation using geometric deformable models and metaheuristics', *Comput. Med. Imaging Graph. Off. J. Comput. Med. Imaging Soc.*, vol. 43, Jan. 2014, doi: 10.1016/j.compmedimag.2013.12.005.

[59] S. F. Gibson and B. Mirtich, 'A Survey of Deformable Modeling in Computer Graphics', 1997.

[60] W. Xu, K. Zhou, Y. Yu, Q. Tan, Q. Peng, and B. Guo, 'Gradient Domain Editing of Deforming Mesh Sequences', in *ACM SIGGRAPH 2007 Papers*, in SIGGRAPH '07. New York, NY, USA: Association for Computing Machinery, 2007, pp. 84-es. doi: 10.1145/1275808.1276482.

[61] Y. Weng, W. Xu, Y. Wu, K. Zhou, and B. Guo, '2D shape deformation using nonlinear least squares optimization', *Vis. Comput.*, vol. 22, pp. 653–660, Sep. 2006, doi: 10.1007/s00371-006-0054-y.

[62] J. Huang *et al.*, 'Subspace Gradient Domain Mesh Deformation', *ACM Trans Graph*, vol. 25, pp. 1126–1134, Jul. 2006, doi: 10.1145/1141911.1142003.

[63] F. Martignac, 'Utilisation de deux outils hydroacoustiques pour analyser la dynamique migratoire du saumon atlantique (*Salmo salar L.*) dans deux fleuves de la baie du Mont-Saint-Michel', PhD Thesis, 2016. [Online]. Available: http://www.theses.fr/2016NSARH097/document

[64] J. Guillard and A. Lebourges-Dhaussy, 'À l'écoute des bancs de poissons', *Pour Sci.*, no. 436, 2014, [Online]. Available: https://hal.science/hal-02549369

[65] J. Serra, *Image Analysis and Mathematical Morphology*. USA: Academic Press, Inc., 1983.

[66] O. Sorkine, D. Cohen-Or, Y. Lipman, M. Alexa, C. Roessl, and H.-P. Seidel, 'Laplacian Surface Editing.', in *ACM International Conference Proceeding Series*, Jul. 2004, pp. 179–188. doi: 10.1145/1057432.1057456.

[67] M. Floater, 'Mean Value Coordinates', *Comput. Aided Geom. Des.*, vol. 20, pp. 19–27, Mar. 2003, doi: 10.1016/S0167-8396(03)00002-5.

[68] R. Larsen, H. Olafsdottir, and B. Ersbøll, 'Shape and Texture Based Classification of Fish Species', Jul. 2009, pp. 745–749. doi: 10.1007/978-3-642-02230-2_76.

[69] H. Eguiraun, K. López-de-Ipiña, and I. Martinez, 'Application of entropy and fractal dimension analyses to the pattern recognition of contaminated fish responses in aquaculture', *Entropy*, vol. 16, no. 11, pp. 6133–6151, 2014.

AZÉNOR LE QUINIO received a diploma in Digital and Healthcare Engineering from the Paris Institute of Digital Technology (ISEP), France, in 2019 and a Ph.D. degree in Statistics/Modelling in Ecology from Institut Agro Rennes-Angers, Rennes, France, in 2023. Her Ph.D. focused on developing computer-vision methods to analyse acoustic videos automatically to detect and track fish and identify species. She currently works as a research engineer in computer vision and signal processing at EDF R&D, Chatou, France. Her current research interests include non-destructive testing of industrial components in the field of energy.

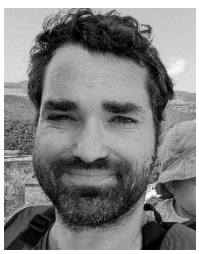

FRANÇOIS MARTIGNAC received an M.S. degree in Ecology and Management of Aquatic Ecosystems from the University of Rennes 1, France, in 2009. From 2010-2017, he was an engineer in a consulting company in Nantes, France, assessing the biological quality of freshwater ecosystems by studying biodiversity in multiple biological compartments. From 2013-2016, his Ph.D. work focused on the migration dynamics of anadromous Atlantic salmon in rivers using different hydroacoustic devices, in collaboration with the INRAE units CARRTEL, in Thonon-les-Bains, France, and DECOD, in Rennes, France. Since 2019, he has been a Research Engineer at the DECOD unit as a specialist in hydrobiology and hydroacoustic methods. His research focuses on diadromous fish populations in rivers using non-intrusive methods, such as sonar imaging, and the development and dissemination of innovative tools to improve fish population surveys by aquatic ecosystem managers.

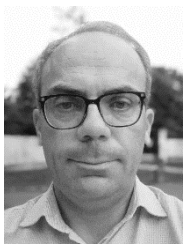

ALEXANDRE GIRARD received an Engineering degree from the Ecole Centrale de Paris, France, in 2000 with a specialisation in applied mathematics. He worked as a consultant in optimisation and robust control of power plants from 2000-2005. He is currently a Research Engineer at EDF in signal and image processing to extract information from non-destructive-testing data and from customer consumption data.

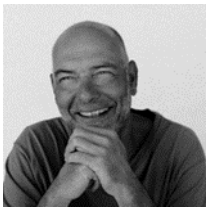

JEAN GUILLARD is a Research Engineer at INRAE, and specialises in applying acoustic methods to study fish populations in aquatic ecosystems. His research encompasses methodological approaches for using these methods (e.g., assessing usage frequency impacts, developing autonomous devices, acoustic cameras) as well as fisheries ecology, including population dynamics, behavioural studies and stock estimates. He has worked in marine, estuarine and especially lacustrine ecosystems, which are central to the research themes of his unit: UMR CARRTEL (INRAE - UMSB). A former director of the unit, he has engaged in many collective projects throughout his career. Additionally, he has directed multiple research and Ph.D. projects that focus on fish populations in lacustrine ecosystems and address topics such as stress ecology, population dynamics and fisheries ecology.

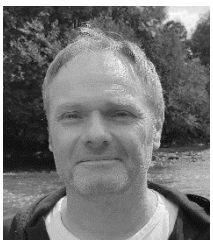

JEAN-MARC ROUSSEL has worked in aquatic ecology for 30 years. After graduating from the University of Rennes (France) with a Ph.D. in Environmental Sciences, he completed post-doctoral studies at the University of Fredericton (New Brunswick, Canada). He is director of research at INRAE and associated researcher at the French Biodiversity Agency (OFB). His expertise includes population and community ecology in temperate and tropical ecosystems, with particular interest in species of high conservation value such as diadromous fish. He leads applied research programs on biodiversity and ecological services associated with aquatic ecosystems and ways to restore them. Since 2012, he has led a multidisciplinary research programme on the Sélune River in France that aims to understand the ecological restoration of the river and its valley after the removal of two large dams (https://programme-selune.com/programme-selune-eng). He has published more than 80 peer-reviewed articles in scientific journals (https://orcid.org/0000-0002-6301-3234).

ERIC DE OLIVEIRA received a Ph.D. degree in 2003 on fish-stock assessment with a focus on geostatistical approaches. As a post-doctoral researcher, he worked in an Interreg Project at IFREMER to develop a method and model to predict seabed habitat distribution. From 1996-1998, he worked on a subantarctic island (Crozet Archipelago), in charge of the field activities of the project "Biodiversity evaluation and ecosystem transformation in a subantarctic island". He joined EDF R&D in 2005 as research engineer in biology. He is involved in two domains: fish passage at a hydropower plant and the latter's impacts on the marine environment. With other departments in the EDF Lab., he has developed new environmental monitoring systems, such as remote sensing of seabed habitats and acoustic methods to detect and quantify the flow of fish in rivers.